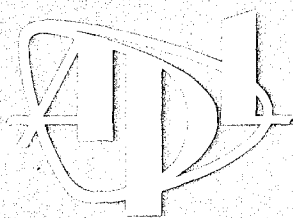


A Model for Bistatic Scattering into Ocean Sediments for Frequencies from 10 – 100 kHz

by Kevin L. Williams and Darrell R. Jackson

Technical Report
APL-UW TR 9505
June 1996

19960627 012



Applied Physics Laboratory, University of Washington
Seattle, Washington 98105-3698

Contract No. N00039-91-C-0072

DATE QUALITY INSPECTED 1

SUPPLEMENTARY

INFORMATION



Applied Physics Laboratory
College of Ocean and Fishery Sciences, University of Washington

ERRATA

2 July 1996

To: Distribution List


From: Nancy L. Penrose, Publications Manager

Subj: Correction to APL-UW Technical Report 9505

Encl: (1) "A Model for Bistatic Scattering into Ocean Sediments for Frequencies from 10 – 100 kHz," by Kevin Williams and Darrell R. Jackson

Please note that there are typographical errors on pages 9 and 10 of APL-UW Technical Report 9505. Corrected pages are enclosed.

The error on page 9 occurs in Equation 31 in the numerator of the term that is multiplied by the factor of 10. The error on page 10 occurs in the term from Equation 31 in the first line of the first paragraph.


Nancy L. Penrose

AD-A310090
19960627012

$$q = \frac{(k|\Delta_z|)^2}{2} C_h^2 (k\Delta_t)^{-2\alpha}, \quad (25)$$

$$\Delta^2 = \{ (-\kappa^2 + \kappa \sin\theta_i \sin\theta_s + \kappa \cos\theta_s \cos\theta_i \cos\phi_s) + \rho \frac{(2-T)}{T} (1 - \kappa \sin\theta_i \sin\theta_s - \kappa \cos\theta_s \cos\theta_i \cos\phi_s) \}, \quad (26)$$

$$\Delta_z = (\kappa \sin\theta_s - \sin\theta_i), \quad (27)$$

$$\Delta_t = \left(\cos^2\theta_i - \frac{2}{v} \cos\theta_i \cos\theta_s \cos\phi_s + \frac{1}{v^2} \cos^2\theta_s \right)^{0.5}. \quad (28)$$

In Eq. 24, $J_0(u)$ is the zeroth-order Bessel function of the first kind. The function $T(\xi)$ is the complex plane-wave transmission coefficient and is related to the reflection coefficient of Eq. 6 by

$$T(\xi) = 1 + R(\xi). \quad (29)$$

This transmission coefficient is evaluated at the complex angle

$$\xi = \text{acos} \left(\left\{ \frac{\kappa^2 [1 - (\sin\theta_i \sin\theta_s + \cos\theta_s \cos\theta_i \cos\phi_s)^2]}{1 + \kappa^2 - 2\kappa (\sin\theta_i \sin\theta_s + \cos\theta_s \cos\theta_i \cos\phi_s)} \right\}^{0.5} \right). \quad (30)$$

This angle was derived by assuming that the local tilt of the surface is such as to give Snell's law transmission in the scattered direction. This is done in analogy with the in-water case, where assuming that the local tilt of the surface is such as to cause specular reflection in the scattered direction gives results closer to "exact" numerical calculations.

Using a procedure similar to that of Jackson (1993), one can approximate the result in Eq. 24 as

$$\sigma_{kr}(\theta_s, \phi_s, \theta_i) = \frac{|T(\xi)|^2}{8\pi} (|\Delta^2|^2 b q_c) \left[\frac{\left(1 + 10 \frac{(\Delta_t^4 + |\Delta_z|^4)}{|\Delta^2|^2} \right)}{(\Delta_t^{4\alpha} + a q_c^2 |\Delta_z|^4)^{\frac{1+\alpha}{2\alpha}}} \right], \quad (31)$$

where

$$q_c = \frac{1}{2} C_h^2 (k)^{2(1-\alpha)}, \quad (32)$$

$$a_o = \left[\frac{8\alpha^2 \Gamma\left(\frac{1+\alpha}{2\alpha}\right)}{\Gamma\left(\frac{1}{\alpha}\right) \Gamma\left(\frac{1}{2}\right) \Gamma\left(\frac{1}{2\alpha}\right)} \right]^{2\alpha}, \quad (33)$$

and

$$b = \left(\frac{a_o^{\frac{1+\alpha}{2\alpha}}}{2\alpha} \right) \Gamma\left(\frac{1}{\alpha}\right). \quad (34)$$

The term $10 (\Delta_t^4 + |\Delta_z|^4) / |\Delta^2|^2$ in Eq. 31 artificially increases the Kirchhoff contribution away from the Snell's law (refraction) direction. Since Eq. 23 favors the smaller of the Kirchhoff and perturbation approximations, this suppresses the Kirchhoff contribution except near the refraction direction.

3.1.2. Perturbation Theory Cross Section

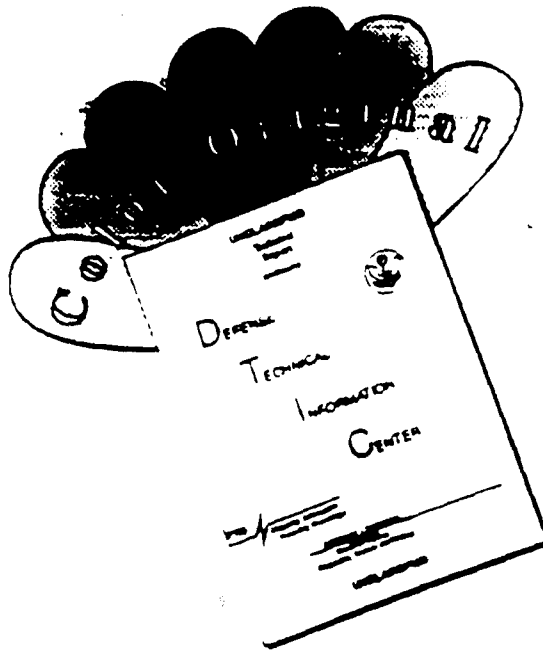
The perturbation-theory results are simplifications of those presented by Moe et al. (1995). In particular, the sediment below the rough interface is assumed to be nonlayered. The resulting cross section is

$$\sigma_{pr}(\theta_s, \phi_s, \theta_i) = A(k, \theta_s) \left| a_1 [1 + R(\theta_i)] + b_1 [1 - R(\theta_i)] \right|^2 W(\Delta_{tr}), \quad (35)$$

where

$$A(k, \theta_s) = \left(\frac{k^4}{4v^2} \right) \left(\frac{\sin^2 \theta_s}{\cos^2 \theta_s} \right) \left| \bar{T}(\theta_s) \right|^2, \quad (36)$$

DISCLAIMER NOTICE



THIS DOCUMENT IS BEST QUALITY AVAILABLE. THE COPY FURNISHED TO DTIC CONTAINED A SIGNIFICANT NUMBER OF COLOR PAGES WHICH DO NOT REPRODUCE LEGIBLY ON BLACK AND WHITE MICROFICHE.

A Model for Bistatic Scattering into Ocean Sediments for Frequencies from 10 – 100 kHz

by Kevin L. Williams and Darrell R. Jackson

Technical Report
APL-UW TR 9505
June 1996



Applied Physics Laboratory University of Washington
1013 NE 40th Street Seattle, Washington 98105-6698

Contract No. N00039-91-C-0072

ACKNOWLEDGMENTS

This work was sponsored by Office of Naval Research Code 321 with direction from the NSWC Coastal Systems Station, Panama City. It was managed by Jim Christoff and Gary Sammelmann under SPAWAR Contract N00039-91-C-0072. The authors are indebted to John Moe for technical discussion and for the use of his surface-perturbation results in development of the model described in this document.

ABSTRACT

A model is developed for bistatic scattering into ocean sediments by an acoustic source located in the water and a receiver buried in the bottom. The model is closely related to that developed by Jackson (1993) for a source and receiver that were both located in the water and parallels that effort in many regards. In particular, bottom scattering is treated as being due to interface roughness and volume inhomogeneity. Kirchhoff theory is used to explain interface scattering near the refracted (Snell's law) direction, and perturbation theory (Moe et al., 1995) is used for all other directions. Perturbation theory is used to treat the scattering due to volume inhomogeneities. Model results are presented for two of the bottom sites examined by Jackson (1993), and possible experimental tests of the model are discussed briefly.

EXECUTIVE SUMMARY

This report describes a model of high-frequency (10–100 kHz) bistatic bottom scattering for an acoustic source located in the water column and a receiver buried in the bottom sediment (referred to here as in-sediment scattering). The physics incorporated into the model has much in common with previous modeling of bistatic scattering done at the Applied Physics Laboratory, University of Washington, the major differences being that in the previous work both the source and the receiver were located in the water column (referred to here as the in-water case). The sediment is treated as a lossy fluid. The bistatic scattering is hypothesized to be due to scattering from interface roughness and from volume inhomogeneities within the sediment. Interface scattering is calculated via the Kirchhoff approximation for angles near the Snell's law direction and via perturbation theory for all other directions. Volume perturbation theory is used to relate bistatic volume scattering to three-dimensional spectra describing fluctuations in sediment density and compressibility.

The input parameters needed (and measured) for the in-sediment model are the same as those used for the in-water case with the addition of one parameter used to give a low-frequency cutoff to the spectra of the volume inhomogeneities. This low-wavenumber cutoff is required to prevent volume-perturbation theory from predicting unrealistically large scattering near the forward-scattering direction. The other parameters are the sediment/water sound-speed ratio, the sediment/water density ratio, two parameters that define the two-dimensional interface relief spectrum, and three parameters that characterize the three-dimensional spectra describing fluctuations in sediment density and compressibility.

One of the attributes of the model is that it predicts penetration of acoustic energy into the sediment at "post-critical" angles, i.e., grazing angles less than the critical angle predicted for a sediment with a sound speed greater than that in water. There has been evidence of post-critical penetration for several years (Chotiros, 1995), but the mechanism involved is still a subject of research. In this model, diffraction, as calculated via surface-interface-perturbation theory, is responsible for most of this post-critical penetration. In fact, the perturbation model adopted here has been used to examine the experimental evidence of post-critical penetration (Moe et al., 1995). The conclusion at this point is that this mechanism predicts results consistent with those experiments.

TABLE OF CONTENTS

	<i>Page</i>
1. INTRODUCTION.....	1
2. DEFINITIONS	1
2.1 Geometry.....	1
2.2 Model Inputs	3
3. BISTATIC SCATTERING CROSS SECTIONS.....	8
3.1 Surface Roughness Scattering.....	8
3.1.1 Kirchhoff Cross Section.....	8
3.1.2 Perturbation Theory Cross Section.....	10
3.2 Volume Scattering	11
4. MODEL ILLUSTRATION AND EXPERIMENTAL TESTS.....	13
4.1 Scattering Strength vs Angle	13
4.2 Scattering Strength vs Position	18
4.3 Experimental Tests of Scattering Strength Model.....	26
5. SUMMARY AND FUTURE DIRECTIONS.....	27
6. REFERENCES	28
7. APPENDIX, Definition of Bistatic Cross Section	29

LIST OF FIGURES

	<i>Page</i>
Figure 1. Bistatic scattering geometry.	2
Figure 2. Model predictions of bistatic scattering strength at 40 kHz for Quinault site as a function of scattered grazing angle, with the incident grazing angle fixed at 90° and the bistatic angle fixed at 180°.....	14
Figure 3. Model predictions of bistatic scattering strength at 40 kHz for Quinault site as a function of scattered grazing angle, with incident grazing angle fixed at 45° and bistatic angle fixed at 180°.	14
Figure 4. Model predictions of bistatic scattering strength at 40 kHz for Quinault site as a function of scattered grazing angle, with incident grazing angle fixed at 10° and bistatic angle fixed at 180°.	15
Figure 5. Model predictions of bistatic scattering strength at 40 kHz for Arafura site as a function of scattered grazing angle, with incident grazing angle fixed at 90° and bistatic angle fixed at 180°.	15
Figure 6. Model predictions of bistatic scattering strength at 40 kHz for Arafura site as a function of scattered grazing angle, with incident grazing angle fixed at 45° and bistatic angle fixed at 180°.	16
Figure 7. Model predictions of bistatic scattering strength at 40 kHz for Arafura site as a function of scattered grazing angle, with incident grazing angle fixed at 10° and bistatic angle fixed at 180°.	16
Figure 8. Scattering strength at 40 kHz as a function of position for specified source and receiver positions, Quinault site.	19
Figure 9. Scattering strength of Figure 8 minus attenuation for the distance traveled from each surface position to the receiver.	19
Figure 10. Scattering strength at 40 kHz as a function of position for specified source and receiver positions, Quinault site.	20
Figure 11. Scattering strength of Figure 10 minus attenuation for the distance traveled from each surface position to the receiver.	20
Figure 12. Scattering strength at 40 kHz as a function of position for specified source and receiver positions, Quinault site.	21
Figure 13. Scattering strength of Figure 12 minus attenuation for the distance traveled from each surface position to the receiver.	21

Figure 14. Scattering strength at 40 kHz as a function of position for specified source and receiver positions, Arafura site.	22
Figure 15. A high-resolution view of the boxed region in Figure 14.	22
Figure 16. Scattering strength of Figure 14 minus attenuation for the distance traveled from each surface position to the receiver.	23
Figure 17. A high-resolution view of the boxed region in Figure 16.	23
Figure 18. Scattering strength at 40 kHz as a function of position for specified source and receiver positions, Arafura site.	24
Figure 19. Scattering strength of Figure 18 minus attenuation for the distance traveled from each surface position to the receiver.	24
Figure 20. Scattering strength at 40 kHz as a function of position for specified source and receiver positions, Arafura site.	25
Figure 21. Scattering strength of Figure 20 minus attenuation for the distance traveled from each surface position to the receiver.	25

LIST OF TABLES

	<i>Page</i>
Table 1. Model input parameters.....	3
Table 2. Model input parameters for Quinault and Arafura Sea sites.....	13

1. INTRODUCTION

The model presented here borrows heavily from the bistatic model of Jackson (1993). Both the physical mechanisms incorporated into the model and the environmental parameters needed as model inputs are the same. The difference is that here the goal is to determine the scattering into the sediment (referred to as in-sediment bistatic scattering) whereas Jackson was interested in determining the scattering into the water column (referred to as in-water bistatic scattering).

The variables and form of the equations have been chosen so as to closely parallel the previous, in-water case. However, the detailed expressions for any particular variable may be different. Section 2 contains some basic definitions and defines the input parameters. Section 3 gives the expressions for both the roughness and the volume-scattering portions of the model. Section 4 presents sample results for two sites (Quinault and Arafura Sea) that were also examined by Jackson (1993) and briefly discusses an experimental test of the model that could be carried out. Section 5 is a summary.

2. DEFINITIONS

The bistatic scattering strength will be written in the form

$$S_b(\theta_s, \phi_s, \theta_i) = 10 \log [\sigma_{br}(\theta_s, \phi_s, \theta_i) + \sigma_{bv}(\theta_s, \phi_s, \theta_i)] , \quad (1)$$

where log is base 10 and $\sigma_{br}(\theta_s, \phi_s, \theta_i)$ and $\sigma_{bv}(\theta_s, \phi_s, \theta_i)$ are, respectively, the roughness and volume contributions to the scattering cross section per unit area. The definition of scattering cross section implicit in the results given here is slightly different than that conventionally used. This definition is given in the appendix.

2.1 Geometry

The angles θ_s , ϕ_s , and θ_i in Eq. 1 are defined in Figure 1; θ_i is the incident grazing angle, θ_s is the scattered grazing angle, and ϕ_s is the bistatic angle defined as the difference in azimuth between the incident and scattered angles. In general, one needs *four* angles, two grazing angles and two azimuthal angles, but only the azimuthal difference is needed here because bottom statistics are assumed to be transversely isotropic.

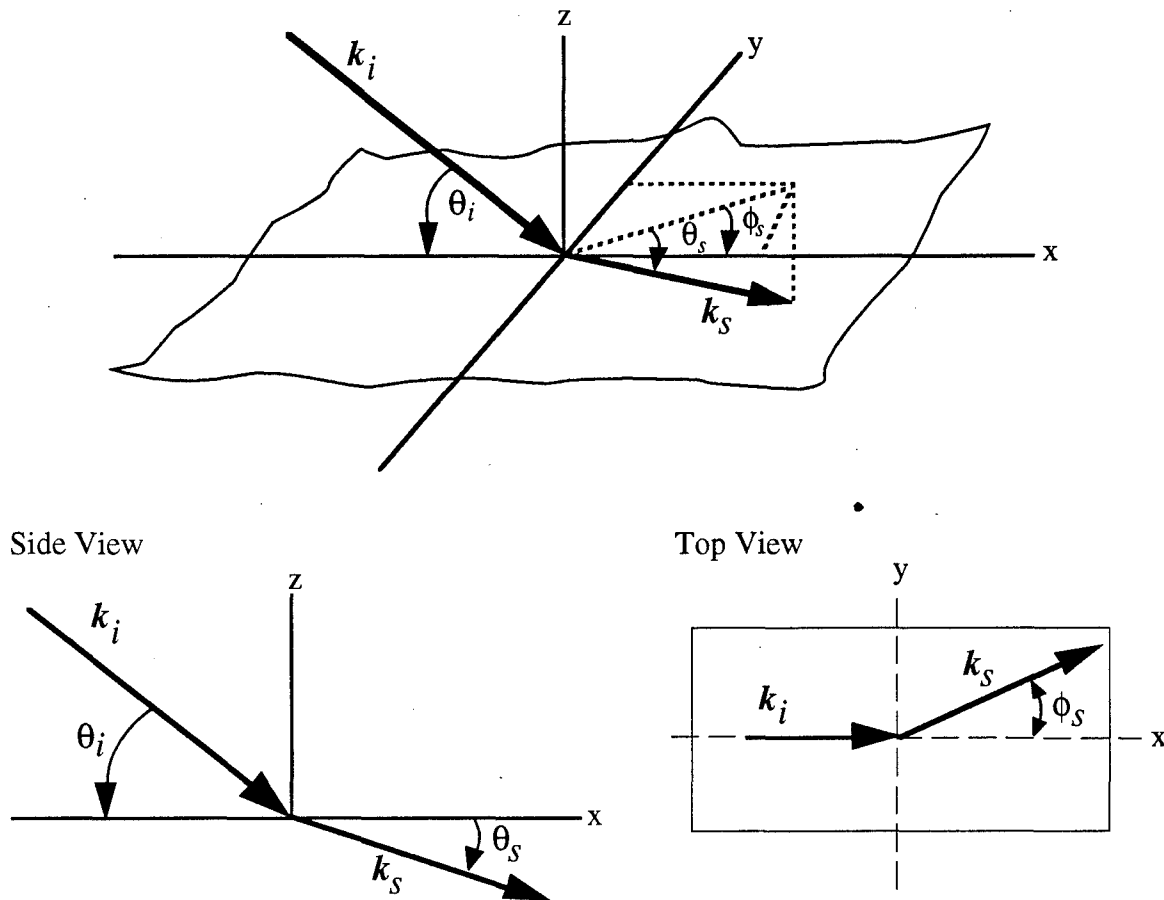


Figure 1. Bistatic scattering geometry. The incident grazing angle is denoted θ_i , the scattered grazing angle is denoted θ_s , and the bistatic angle, defined as the difference in azimuth between the incident and scattered directions, is denoted ϕ_s .

The vectors \mathbf{k}_i and \mathbf{k}_s are also shown in Figure 1. These vectors are the incident and scattered wave vectors, respectively. From Figure 1, we have

$$\mathbf{k}_i = k (\hat{x} \cos \theta_i - \hat{z} \sin \theta_i) \quad (2)$$

and

$$\mathbf{k}_s = k_b [\hat{x} (\cos \theta_s \cos \phi_s) + \hat{y} (\cos \theta_s \sin \phi_s) - \hat{z} \sin \theta_s], \quad (3)$$

where k is the acoustic wavenumber in the water and k_b is the (complex) acoustic wavenumber in the sediment.

2.2 Model Inputs

The input parameters for the bistatic bottom-scattering model are given in Table 1. Procedures have been developed to provide estimates of these parameters when direct physical measurements are lacking (Mourad and Jackson, 1989). The bottom material is treated as a fluid with no layering or gradients (apart from the random fluctuations responsible for volume scattering). The density ratio, sound-speed ratio, and loss parameter characterize the nonrandom acoustic properties of the sediment. It is convenient to define the following complex quantities in terms of these parameters (Mourad and Jackson, 1989).

$$\kappa = \frac{1 + i\delta}{v}, \quad (4)$$

$$P(\theta) = \sqrt{\kappa^2 - \cos^2 \theta}, \quad (5)$$

Table 1. Model input parameters. Also needed are values for frequency, water sound speed, and water-mass density.

Symbol	Definition	Short Name
ρ	Ratio of sediment mass density to water mass density	Density ratio
v	Ratio of sediment sound speed to water sound speed	Sound-speed ratio
δ	Ratio of imaginary wavenumber to real wavenumber for the sediment	Loss parameter
γ_3	Exponent of sediment inhomogeneity spectrum	Inhomogeneity exponent
w_3	Strength of sediment inhomogeneity spectrum (cm^3) at wavenumber $(2\pi)/\lambda = 1 \text{ cm}^{-1}$	Inhomogeneity strength
μ	Ratio of compressibility to density fluctuations in the sediment	Fluctuation ratio
γ_2	Exponent of the bottom relief spectrum	Spectral exponent
w_2	Strength of bottom relief spectrum (cm^4) at wavenumber $(2\pi)/\lambda = 1 \text{ cm}^{-1}$	Spectral strength
a	Low-wavenumber cutoff parameter for sediment inhomogeneity spectrum (cm)	Cutoff parameter

and

$$R(\theta) = \frac{(\rho \sin \theta) / [P(\theta)] - 1}{(\rho \sin \theta) / [P(\theta)] + 1}. \quad (6)$$

In Eq. 5, the quantity inside the square root is complex, and the square root is defined as the complex number whose magnitude is the positive square root of the original magnitude and whose angle is one-half the original angle. The quantity $P(\theta)$, defined by Eq. 5, is the normalized z component of the wave vector in the sediment for an incoming plane wave having grazing angle θ in the water. This definition assumes that the bottom is perfectly flat and homogeneous, although the scattering models to be used later do not. The normalization is simply division by k , the acoustic wavenumber in the water. Finally, $R(\theta)$ is the flat-interface Rayleigh reflection coefficient. The complex quantities $P(\theta)$ and $R(\theta)$ will appear in later expressions for the roughness and sediment volume-scattering cross sections. The quantity κ is the ratio of the acoustic wavenumber in the sediment (a complex number) to the acoustic wavenumber in the water (a real number). The loss parameter, δ , can be obtained in terms of the more commonly defined sediment sound absorption coefficient, α_b , as follows:

$$\delta = \frac{\alpha_b v c \ln 10}{40\pi f}. \quad (7)$$

Care must be exercised in the choice of units here. If α_b is in units of decibels per meter, as is usually the case, and the water sound speed, c , is in meters per second, then the acoustic frequency, f , must be in hertz.

The density ratio, sound-speed ratio, and loss parameters are identical to those used by Mourad and Jackson (1989) in their backscatter model, as are the two parameters used to describe random bottom relief (also referred to as bottom roughness). Bottom relief is assumed to be a Gaussian random process having the following two-dimensional spectrum:

$$W(K) = \frac{w_2}{(Kh_0)^{\gamma_2}}. \quad (8)$$

In this expression, w_2 and γ_2 are model parameters for the strength and exponent of the relief spectrum, and h_0 is simply a reference length equal to 1 cm. The subscript "2" denotes

the fact that bottom relief is a two-dimensional random process. Since the relief spectrum depends only on the magnitude of the two-dimensional wave vector, ($K = |\mathbf{K}|$), bottom relief is assumed to be isotropic. We will use upper-case letters (e.g., \mathbf{K}) to denote transverse vectors. The spectrum is normalized so that

$$2\pi \int_{K_c}^{\infty} W(K) K dK = h^2(K_c). \quad (9)$$

In this expression, $h^2(K_c)$ is the mean-square roughness due to those Fourier components of bottom relief having a wavenumber greater than K_c . The wavenumber K_c can be viewed as a cutoff on the spectrum. It is an independent variable employed to yield finite values for mean-square roughness. The spectral exponent is constrained as follows:

$$2 < \gamma_2 < 4. \quad (10)$$

The relief statistics can be alternately described by the "structure function" (Yaglom, 1962), itself a power law if the spectrum is a power law:

$$D(R) = \langle [f(\mathbf{R}_0 + \mathbf{R}) - f(\mathbf{R}_0)]^2 \rangle = C_h^2 R^{2\alpha}, \quad (11)$$

where $f(R)$ is the z coordinate of the interface at horizontal position $\mathbf{R} = (x, y)$. The function $f(\mathbf{R})$ is a zero-mean, two-dimensional Gaussian random process. The structure function parameters are related to the spectrum parameters as follows:

$$\alpha = \frac{\gamma_2}{2} - 1 \quad (12)$$

and

$$C_h^2 = \frac{2\pi w_2 \Gamma(2 - \alpha) 2^{-2\alpha}}{h_0^{\gamma_2} \alpha (1 - \alpha) \Gamma(1 + \alpha)}, \quad (13)$$

where Γ is the gamma function.

The four new parameters (γ_3 , w_3 , μ , and a) used in the in-sediment (and in-water) bistatic model but not in earlier monostatic models describe three-dimensional sediment inhomogeneity. These replace a single volume-scattering parameter appearing in the older monostatic

models. Sediment inhomogeneities are described by three-dimensional spectra for compressibility and density fluctuations, normalized by dividing by their mean values. We denote these normalized compressibility and density fluctuations by $\gamma_K(\mathbf{r})$ and $\gamma_\rho(\mathbf{r})$, respectively. We assume that the fluctuations in sediment compressibility and density are tied together by a simple proportionality relation,

$$\gamma_K(\mathbf{r}) = \mu \gamma_\rho(\mathbf{r}). \quad (14)$$

In saturated sediments, we expect the model parameter μ to have values in the neighborhood of -1 because density and compressibility tend to be anticorrelated. For example, if a loosening of the sediment produces a 10% *decrease* in density, then there will be a corresponding *increase* of about 10% in compressibility. These two changes must be of about the same magnitude, because it is known that a 10% change in density is likely to produce a much smaller percentage change in sediment sound speed, c_b . Since

$$c_b = \frac{1}{\sqrt{\rho_b K_b}}, \quad (15)$$

it follows that density and compressibility changes must be anticorrelated in order to produce a small change in sound speed. (See Hamilton and Bachman (1982) and Richardson and Briggs (1993) for data on the relationship between density and sound speed.)

We assume that the fluctuations in density and compressibility are spatially stationary, so that power spectra can be defined as Fourier transforms of the corresponding fluctuation covariances.

$$W_{\rho\rho}(k_v) = \frac{1}{(2\pi)^3} \int e^{-ik_v \cdot \mathbf{r}} \langle \gamma_\rho(\mathbf{r}_0 + \mathbf{r}) \gamma_\rho(\mathbf{r}_0) \rangle d^3\mathbf{r}, \quad (16)$$

$$W_{KK}(k_v) = \frac{1}{(2\pi)^3} \int e^{-ik_v \cdot \mathbf{r}} \langle \gamma_K(\mathbf{r}_0 + \mathbf{r}) \gamma_K(\mathbf{r}_0) \rangle d^3\mathbf{r}, \quad (17)$$

$$W_{\rho K}(k_v) = \frac{1}{(2\pi)^3} \int e^{-ik_v \cdot \mathbf{r}} \langle \gamma_\rho(\mathbf{r}_0 + \mathbf{r}) \gamma_K(\mathbf{r}_0) \rangle d^3\mathbf{r}. \quad (18)$$

We assume that the spectrum for density fluctuations obeys the following power law:

$$W_{\rho\rho}(k_v) = \frac{w_3}{(k_v h_0)^{\gamma_3}} \{1.0 - \exp[-(k_v a)^2/2]\}^2. \quad (19)$$

Equation 14 then forces the following expressions for the compressibility fluctuation spectrum, $W_{KK}(k_v)$, and the cross spectrum, $W_{\rho K}(k_v)$:

$$W_{KK}(k_v) = \frac{w_3 \mu^2}{(k_v h_0)^{\gamma_3}} \{1.0 - \exp[-(k_v a)^2/2]\}^2 \quad (20)$$

and

$$W_{\rho K}(k_v) = \frac{w_3 \mu}{(k_v h_0)^{\gamma_3}} \{1.0 - \exp[-(k_v a)^2/2]\}^2. \quad (21)$$

For the sake of simplicity, three-dimensional isotropy is assumed for the sediment inhomogeneity. This is reflected in Eqs. 16–21 in that these spectra depend only upon the *magnitude*, k_v , of the three-dimensional wave vector, \mathbf{k}_v . Layered sediments, by definition, do not possess three-dimensional isotropy. It is an open question whether a more complicated, anisotropic sediment model is needed at high frequencies.

The term in braces in Eqs. 19–21 introduces a low k_v cutoff into the spectra. This prevents an unphysical divergence near forward scattering. In the results discussed in this report, a is set to 50 cm. The filtered spectra of Eqs. 19–21 then agree with the unfiltered ones (Eqs. 19–21 without the term in braces) down to $O(1 \text{ m})$. Furthermore, integration of Eq. 19 (for the case $\gamma_3 = 3$) gives

$$\sigma_p^2 = \frac{4\pi w_3}{h_0^3} \left\{ \frac{Ei[-(k_v^2 a^2)]}{2} - Ei\left[-\frac{(k_v^2 a^2)}{2}\right] + \ln(k_v) \right\} \bigg|_{k_v=0}^{k_2} \quad (22)$$

for the density variance, where k_2 is a high-wavenumber cutoff such that the smallest volume inhomogeneities are $O(1 \text{ mm})$ and Ei is the exponential integral function. When this result is evaluated using $a = 50 \text{ cm}$ and the w_3 values for the sediments in Section 4, the standard deviation is less than 0.18, which is consistent with available core density data (Jackson, 1993).

3. BISTATIC SCATTERING CROSS SECTIONS

3.1 Surface Roughness Scattering

In this section, expressions are presented for the bistatic cross sections in the Kirchhoff and perturbation approximations. The net cross section, $\sigma_{br}(\theta_s, \phi_s, \theta_i)$, appearing in Eq. 1 is formed by smooth interpolation between the Kirchhoff cross section near the specular direction and the perturbation-theory cross section elsewhere. The interpolation between these two approximations is defined so that the smaller cross section takes precedence. This procedure is based on the fact that, for power-law spectra, the perturbation approximation overpredicts scattering near the specular direction owing to the singularity in the relief spectrum at zero wavenumber. In contrast, the Kirchhoff approximation tends to overpredict in other directions. The interpolation scheme used here is

$$\sigma_{br}(\theta_s, \phi_s, \theta_i) = [\sigma_{kr}^{\eta}(\theta_s, \phi_s, \theta_i) + \sigma_{pr}^{\eta}(\theta_s, \phi_s, \theta_i)]^{1/\eta}, \quad (23)$$

with $\eta = -2$. The expressions for the Kirchhoff (σ_{kr}) and perturbation-theory (σ_{pr}) cross sections are defined next.

3.1.1. Kirchhoff Cross Section

In analogy with the in-water monostatic expression used by Jackson and Briggs (1992) and the bistatic expression used by Jackson (1993), the Kirchhoff bistatic cross section is

$$\sigma_{kr}(\theta_s, \phi_s, \theta_i) = \frac{|T(\xi)|^2}{8\pi} \left(\frac{|\Delta^2|}{|\Delta_z|\Delta_t} \right)^2 \int_0^\infty e^{-qu^{2\alpha}} J_0(u) u du, \quad (24)$$

where

$$q = \frac{(k|\Delta_z|)^2}{2} C_h^2 (k\Delta_t)^{-2\alpha}, \quad (25)$$

$$\Delta^2 = \{ (-\kappa^2 + \kappa \sin \theta_i \sin \theta_s + \kappa \cos \theta_s \cos \theta_i \cos \phi_s) + \rho \frac{(2-T)}{T} (1 - \kappa \sin \theta_i \sin \theta_s - \kappa \cos \theta_s \cos \theta_i \cos \phi_s) \}, \quad (26)$$

$$\Delta_z = (\kappa \sin \theta_s - \sin \theta_i), \quad (27)$$

$$\Delta_t = \left(\cos^2 \theta_i - \frac{2}{v} \cos \theta_i \cos \theta_s \cos \phi_s + \frac{1}{v^2} \cos^2 \theta_s \right)^{0.5}. \quad (28)$$

In Eq. 24, $J_0(u)$ is the zeroth-order Bessel function of the first kind. The function $T(\xi)$ is the complex plane-wave transmission coefficient and is related to the reflection coefficient of Eq. 6 by

$$T(\xi) = 1 + R(\xi). \quad (29)$$

This transmission coefficient is evaluated at the complex angle

$$\xi = \text{acos} \left(\left\{ \frac{\kappa^2 [1 - (\sin \theta_i \sin \theta_s + \cos \theta_s \cos \theta_i \cos \phi_s)^2]}{1 + \kappa^2 - 2\kappa (\sin \theta_i \sin \theta_s + \cos \theta_s \cos \theta_i \cos \phi_s)} \right\}^{0.5} \right). \quad (30)$$

This angle was derived by assuming that the local tilt of the surface is such as to give Snell's law transmission in the scattered direction. This is done in analogy with the in-water case, where assuming that the local tilt of the surface is such as to cause specular reflection in the scattered direction gives results closer to "exact" numerical calculations.

Using a procedure similar to that of Jackson (1993), one can approximate the result in Eq. 24 as

$$\sigma_{kr}(\theta_s, \phi_s, \theta_i) = \frac{|T(\xi)|^2}{8\pi} (|\Delta^2|^{2b} q_c) \left[\frac{\left(1 + 10 \frac{(\Delta_t^4 |\Delta_z|^4)}{|\Delta^2|^2} \right)}{(\Delta_t^{4\alpha} + a q_c^2 |\Delta_z|^4)^{\frac{1+\alpha}{2\alpha}}} \right], \quad (31)$$

where

$$q_c = \frac{1}{2} C_h^2 (k)^{2(1-\alpha)}, \quad (32)$$

$$a_o = \left[\frac{8\alpha^2 \Gamma\left(\frac{1+\alpha}{2\alpha}\right)}{\Gamma\left(\frac{1}{\alpha}\right) \Gamma\left(\frac{1}{2}\right) \Gamma\left(\frac{1}{2\alpha}\right)} \right]^{2\alpha}, \quad (33)$$

and

$$b = \left(\frac{a_o^{\frac{1+\alpha}{2\alpha}}}{2\alpha} \right) \Gamma\left(\frac{1}{\alpha}\right). \quad (34)$$

The term $10 (\Delta_i^4 + |\Delta_3|^4) / |\Delta^2|^2$ in Eq. 31 artificially increases the Kirchhoff contribution away from the Snell's law (refraction) direction. Since Eq. 23 favors the smaller of the Kirchhoff and perturbation approximations, this suppresses the Kirchhoff contribution except near the refraction direction.

3.1.2. Perturbation Theory Cross Section

The perturbation-theory results are simplifications of those presented by Moe et al. (1995). In particular, the sediment below the rough interface is assumed to be nonlayered. The resulting cross section is

$$\sigma_{pr}(\theta_s, \phi_s, \theta_i) = A(k, \theta_s) |a_1 [1 + R(\theta_i)] + b_1 [1 - R(\theta_i)]|^2 W(\Delta_{tr}), \quad (35)$$

where

$$A(k, \theta_s) = \left(\frac{k^4}{4v^2} \right) \left(\frac{\sin^2 \theta_s}{\cos^2 \theta_s} \right) \left| \bar{T}(\theta_s) \right|^2, \quad (36)$$

$$\bar{T}(\theta_s) = \frac{2\rho \sqrt{1 - \frac{\cos^2 \theta_s}{v^2}}}{\rho \sqrt{1 - \frac{\cos^2 \theta_s}{v^2}} + \sqrt{\kappa^2 - \frac{\cos^2 \theta_s}{v^2}}}, \quad (37)$$

$$a_1 = \left(\frac{1}{\rho} - 1 \right) \frac{\cos \theta_i \cos \theta_s \cos \phi_s}{v} + 1 - \frac{\kappa^2}{\rho}, \quad (38)$$

$$b_1 = \left(\sqrt{1 - \frac{\cos^2 \theta_s}{v^2}} \right) \sin \theta_i (1 - \rho), \quad (39)$$

$$\Delta_{tr} = k (\Delta_t + 0.0001). \quad (40)$$

The expression for W is given in Eq. 8 and that for Δ_t in Eq. 28. The definition in Eq. 40 is used to avoid the singularity in the relief spectrum at zero wavenumber. In practice, the divergence is not a problem since in this regime the Kirchhoff result is used. The term 0.0001 in Eq. 40 simply keeps computer codes from self-destructing.

3.2 Volume Scattering

As in the in-water case, an effective interface-scattering cross section is used that is derived from an integration of the volume scattering in depth. As a note of caution, this procedure may lead to an overprediction of volume scattering near normal incidence. In practice, however, this overprediction will probably not be visible, since, near normal incidence, the Kirchhoff interface scattering is the dominant process in getting energy to the in-sediment receiver. (See Section 4.)

Using conventional volume scattering perturbation theory, Jackson (1993) arrived at an expression for the volume-scattering cross section. The same result applies here.

$$\sigma_v = \frac{\pi |k_b|^4}{2} \left\{ W_{KK}(\Delta_k) + 2 \operatorname{Re} \left[\frac{k_{bi} \cdot k_{bs} (k_b^*)^2}{|k_b|^4} \right] W_{\rho K}(\Delta_k) + \frac{|k_{bi} \cdot k_{bs}|^2}{|k_b|^4} [W_{\rho\rho}(\Delta_k)] \right\}. \quad (41)$$

Using the discussion in Section 2 this can be rewritten as

$$\sigma_v = \frac{\pi |k_b|^4}{2} [W_{\rho\rho}(\Delta_k)] \left(\mu^2 + 2\mu \left\{ \operatorname{Re} \left[\frac{k_{bi} \cdot k_{bs} (k_b^*)^2}{|k_b|^4} \right] \right\} + \frac{|k_{bi} \cdot k_{bs}|^2}{|k_b|^4} \right), \quad (42)$$

where k_{bs} is given in Eq. 3,

$$k_{bi} = \hat{x} k \cos \theta_i - \hat{z} k P(\theta_i), \quad (43)$$

and

$$\Delta k = |\operatorname{Re}(k_{bs}) - \operatorname{Re}(k_{bi})|. \quad (44)$$

Eqs. 42–44 are used in the effective interface cross section

$$\sigma_{bv}(\theta_s, \phi_s, \theta_i) = \sigma_v \left(\frac{|T(\theta_i)|^2}{2 \left[-\delta \frac{k}{v} \sin \theta_s + k \operatorname{Im}(P(\theta_i)) \right]} \right), \quad (45)$$

where T is defined in Eq. 29 and P in Eq. 5.

4. MODEL ILLUSTRATION AND EXPERIMENTAL TESTS

We illustrate the model by employing parameters appropriate to two sites, Quinault and Arafura Sea. The Quinault site has a sandy bottom and is off the coast of Washington State. The Arafura Sea site has a silty bottom and is north of Australia. Table 2 gives the model parameters for both sites.

Table 2. Model input parameters for Quinault and Arafura Sea sites.

Site	Sound-Speed Ratio (v)	Density Ratio (ρ)	Loss Param. (δ)	Inhomo. Expon. (γ_3)	Inhomo. Strength (w_3), cm^3	Fluct. Ratio (μ)	Cutoff Parameter (a), cm	Relief Expon. (γ_2)	Relief Strength (w_2), cm^4
Quinault	1.1130	1.940	0.01150	3.0	0.000127	-1.0	50	3.67	0.00422
Arafura	0.9880	1.390	0.00533	3.0	0.000306	-1.0	50	3.18	0.00318

For these sites, all parameters except those for volume inhomogeneity are taken from Jackson and Briggs (1992). The inhomogeneity exponent, γ_3 , was set to 3. As noted by Jackson and Briggs, this yields a frequency-independent contribution of volume scattering to the effective interface scattering strength, in agreement with available data. The parameter μ , which relates density and compressibility fluctuations, is taken to be -1. The inhomogeneity strength parameter, w_3 , was determined by requiring that the normalized volume-scattering parameter (Eq. 46 of Jackson, 1993) have the value used by Jackson and Briggs. As mentioned earlier, the interpolation parameter, η , was set to -2.

4.1 Scattering Strength vs Angle

Figures 2-7 show predictions of the total bistatic scattering strength and the scattering strength associated with each component of the model as a function of scattered grazing angle, with the incident grazing angle and bistatic angle held fixed. Figures 2-4 are for the Quinault site and Figures 5-7 are for the Arafura site. The goal of this section is both to give results that can be used to check code implementation and to comment on some of the characteristics seen in the figures.

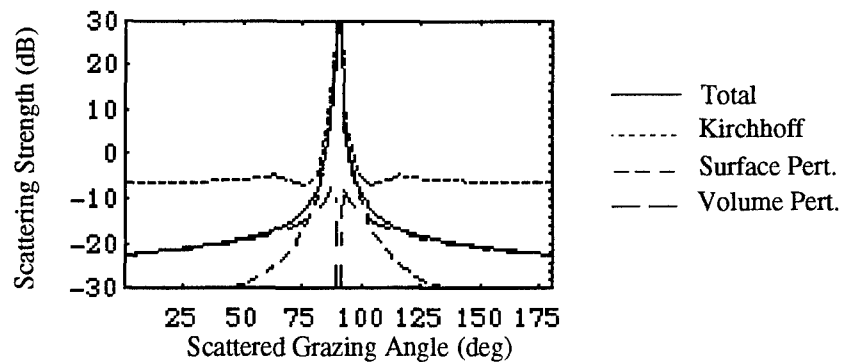


Figure 2. Model predictions of bistatic scattering strength at 40 kHz for Quinault site as a function of scattered grazing angle, with the incident grazing angle fixed at 90° and the bistatic angle fixed at 180° . Separate components and the interpolated total scattering are shown.

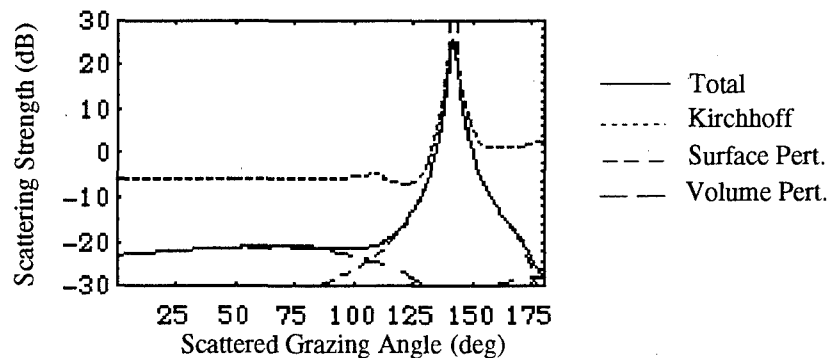


Figure 3. Model predictions of bistatic scattering strength at 40 kHz for Quinault site as a function of scattered grazing angle, with incident grazing angle fixed at 45° and bistatic angle fixed at 180° . Separate components and the interpolated total scattering are shown.

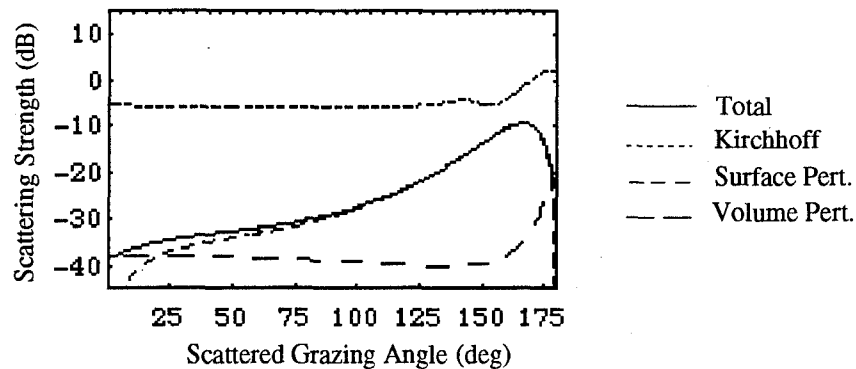


Figure 4. Model predictions of bistatic scattering strength at 40 kHz for Quinault site as a function of scattered grazing angle, with incident grazing angle fixed at 10° and bistatic angle fixed at 180° . Separate components and the interpolated total scattering are shown.

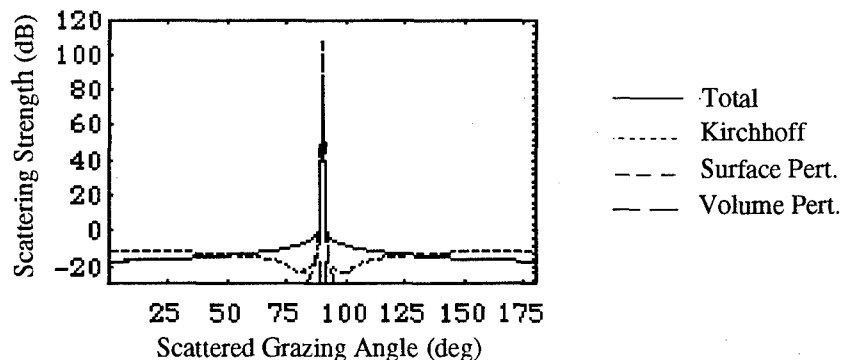


Figure 5. Model predictions of bistatic scattering strength at 40 kHz for Arafura site as a function of scattered grazing angle, with incident grazing angle fixed at 90° and bistatic angle fixed at 180° . Separate components and the interpolated total scattering are shown.

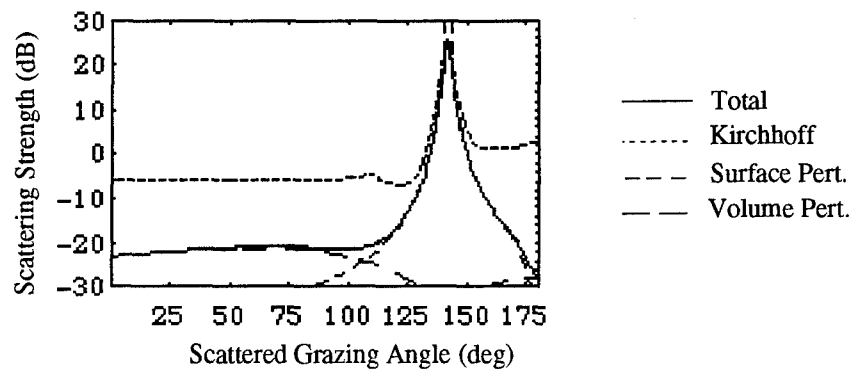


Figure 6. Model predictions of bistatic scattering strength at 40 kHz for Arafura site as a function of scattered grazing angle, with incident grazing angle fixed at 45° and bistatic angle fixed at 180° . Separate components and the interpolated total scattering are shown.

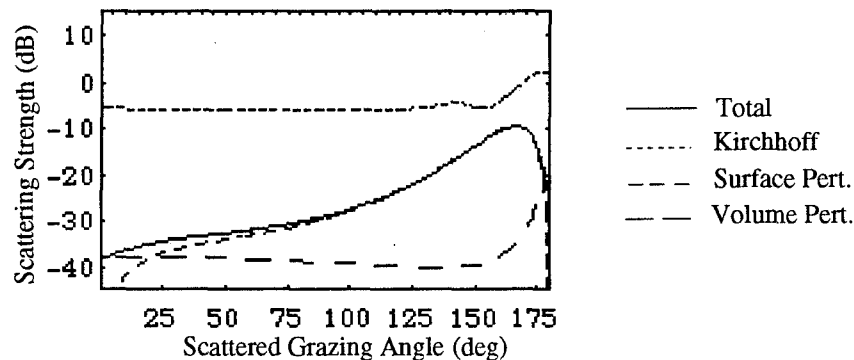


Figure 7. Model predictions of bistatic scattering strength at 40 kHz for Arafura site as a function of scattered grazing angle, with incident grazing angle fixed at 10° and bistatic angle fixed at 180° . Separate components and the interpolated total scattering are shown.

When examining the figures, it is important to remember that the interpolation scheme of Eq. 23 results in the smaller of either the Kirchhoff or the perturbation results being used in calculating the total scattering strength. For the Quinault site, the sound-speed ratio in Table 2 implies the existence of a critical angle of about 26° . Therefore Figures 2 and 3 are for incident angles where a refracted path would be expected for a flat surface. The peak in the scattering strength is at the scattered angle appropriate for a refracted path, and the Kirchhoff approximation is being used to calculate the scattering strength near this (Snell's law) direction. Further away from this direction, the surface-perturbation contribution first comes into play and then the volume-scattering.

The volume-scattering contribution has been approximated in terms of an equivalent surface-scattering cross section (given by Eq. 45); i.e., the denominator in Eq. 45 is a measure of the relative contribution of volume scatterers as a function of depth. In Figure 2, where the incident grazing angle is 90° , the denominator becomes very small near scattered grazing angles of 90° . Physically, this is because the increased attenuation of the incident wave, in propagation from the surface to the scattering volume, is balanced by a decrease in attenuation in propagation from the scattering volume to the receiver. As a result, the present approximation almost certainly overpredicts the volume-scattering strength for these near-normal-incidence geometries. However, since the surface roughness (the Kirchhoff contribution) is the dominating effect for scattered grazing angles near 90° , this overprediction would seem to be of little practical significance. Nevertheless, caution is warranted when using the present model near normal incidence.

Figure 4 is for an incident angle well past critical, so a refracted path into the sediment does not exist and the Kirchhoff approximation never plays a role. The volume-scattering contribution (which results from an evanescent wave in the sediment scattering from volume inhomogeneities) is smaller than the surface-perturbation contribution for all but a small range of scattered angles near backscattering. The results given in Section 4.2 will show that the scattered grazing angles near 90° play an important role in the signal that a buried receiver will see. Near 90° surface perturbation theory, i.e., diffraction due to surface roughness, dominates the scattering process.

For the Arafura site, the sound speed in the sediment is less than that in the water, so no critical angle exists. Figures 5–7 show that the scattering strength peaks in direction of the

refracted path. Furthermore, the surface roughness leads to a much narrower peak in this direction. This will be seen to have ramifications on the figures shown in the following section. Finally, volume scattering plays the major role in the scattering strength away from this narrow peak. The coloring scheme used in the figures masks the blue of volume scattering by the red of total scattering when the two are nearly equal.

4.2 Scattering Strength vs Position

Typically, the scattering strength will be used to calculate the intensity received at a point in the sediment from a source in the water column. This involves an integral over the water/sediment interface in which the integrand includes the scattering cross section at each interface position, spherical spreading from the source to the surface point then from the surface point to the receiver, and attenuation within the sediment. Figures 8–21 present plots of (1) the scattering strength as a function of position, and (2) the integrand in the calculation of received intensity for three source/receiver geometries. The scattering-strength plots indicate the relative levels of intensity that traverse the interface, whereas the integrand plots show how these scattering strengths contribute to the received intensity.

In all the geometries examined, the horizontal separation between the receiver and the point source is 20 m, and the depth of the receiver below the water/sediment interface is 1 m. The heights of the source above the interface are 5, 10, and 20 m. The source and receiver positions are given on each figure in x,y,z format. Figures 8–13 are for the Quinault site, and Figures 14–21 for the Arafura site.

Figures 8, 10, and 12 show the scattered strength as a function of position on the interface for source heights of 20, 10, and 5 m, respectively. As the source is lowered, the elliptical region where the highest intensity is scattered into the sediment elongates, and the peak intensity moves toward the source. The position of the peak corresponds to the refracted path for a flat interface. There is also a secondary maximum in the scattering strength immediately below the source. This is due to volume scattering. Contrast these figures with Figures 9, 11, and 13, which show the relative contributions to the intensity seen at the receiver for source heights of 20, 10, and 5 m. The most significant contributions come from the region immediately above the receiver. This is because sound from that region has the shortest path to traverse within the sediment (and therefore the least attenuation) to arrive at the receiver.

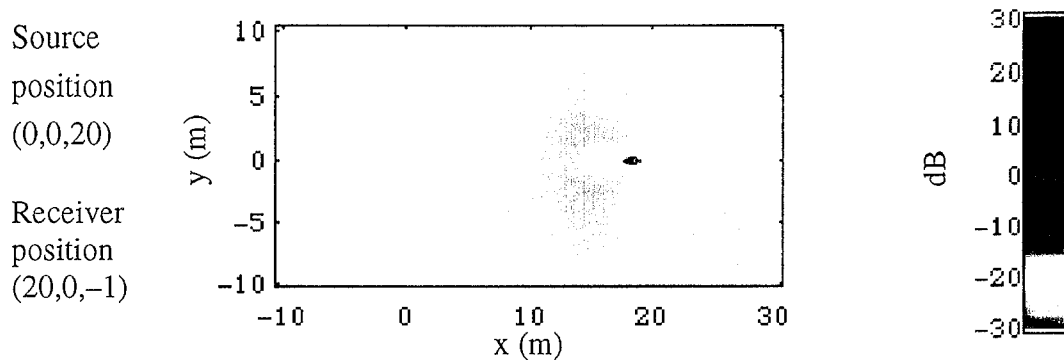


Figure 8. Scattering strength at 40 kHz as a function of position for source and receiver positions given in meters at left (x, y, z), Quinault site. For this geometry, the incident grazing angle immediately above the receiver, i.e., at (20,0,0), is well above the critical angle of 26° .

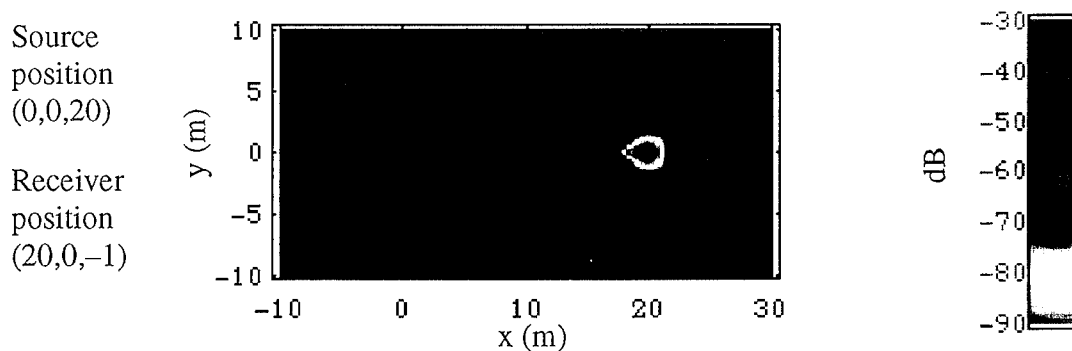


Figure 9. Scattering strength of Figure 8 minus α_b (see Eq. 7) times distance traveled from each surface position to the receiver. The result indicates the major region of the surface contributing to the received energy. All values below -90 dB have been set equal to -90 dB. Note that the majority of the plot is at the red level corresponding to -90 dB.

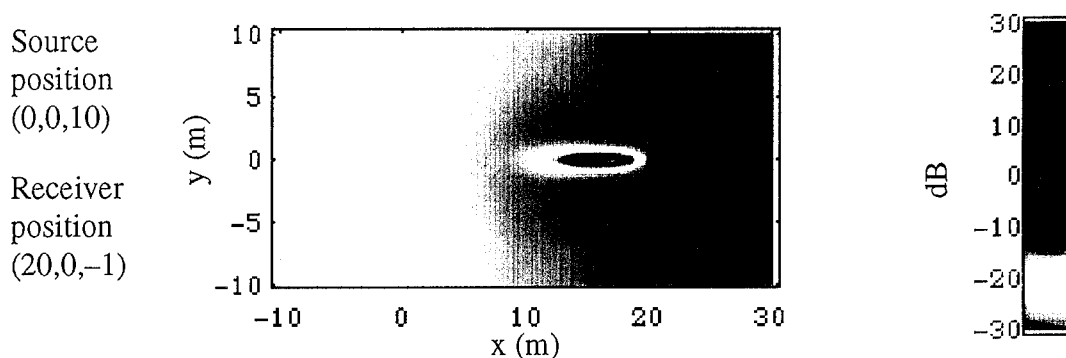


Figure 10. Scattering strength at 40 kHz as a function of position for source and receiver positions given in meters at left (x,y,z), Quinault site. For this geometry, the incident grazing angle of 26.5° immediately above the receiver, i.e., at (20,0,0), is approximately equal to the critical angle of 26° .

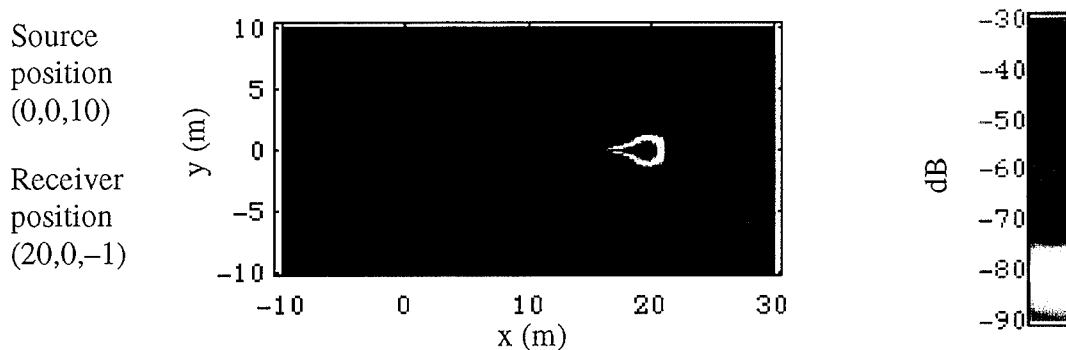
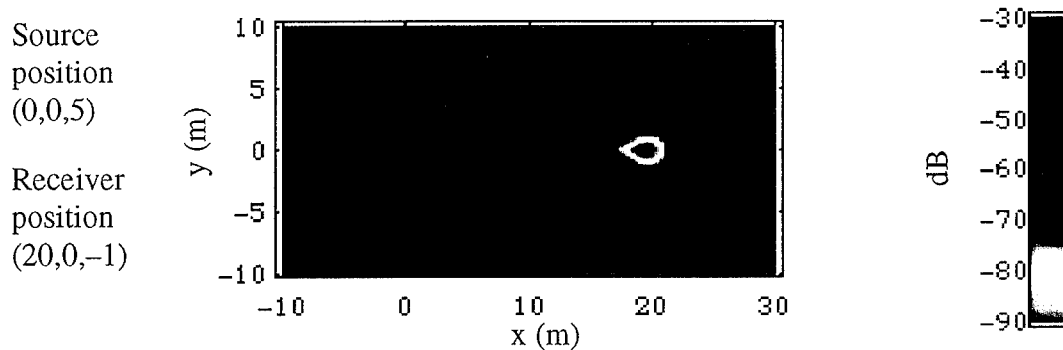
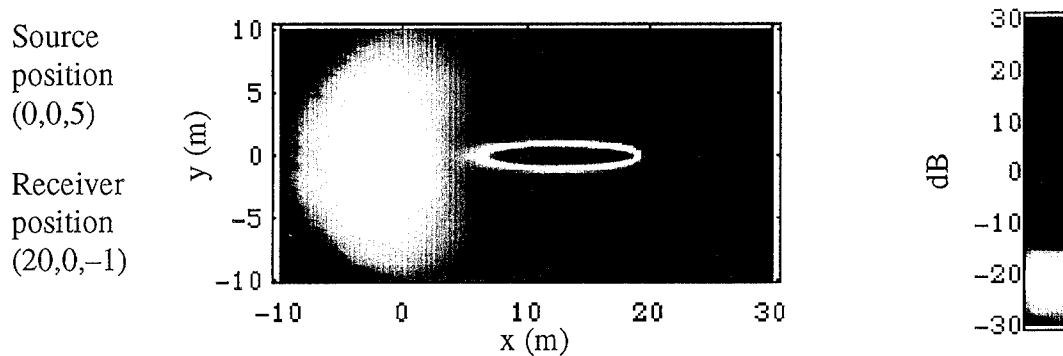


Figure 11. Scattering strength of Figure 10 minus α_p (see Eq. 7) times distance traveled from each surface position to the receiver. The result indicates the major region of the surface contributing to the received energy. All values below -90 dB have been set equal to -90 dB.



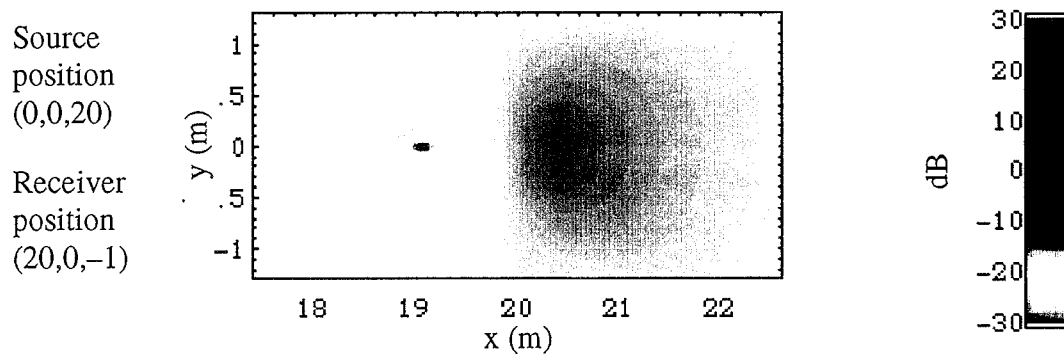
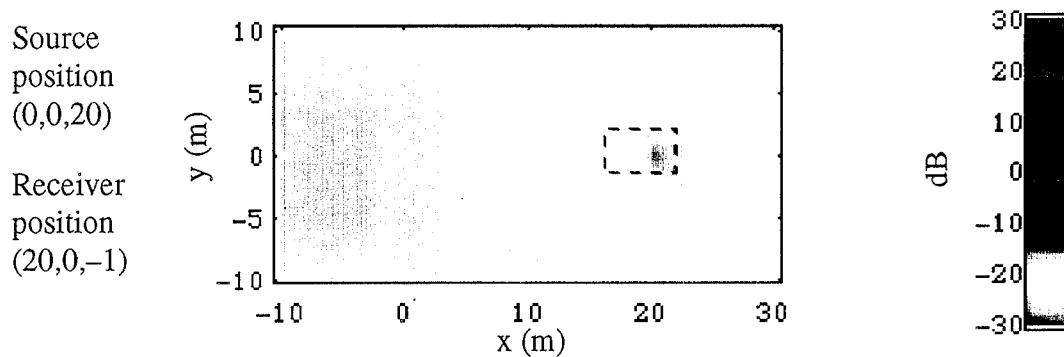


Figure 15. A high-resolution view of the boxed region in Figure 14.

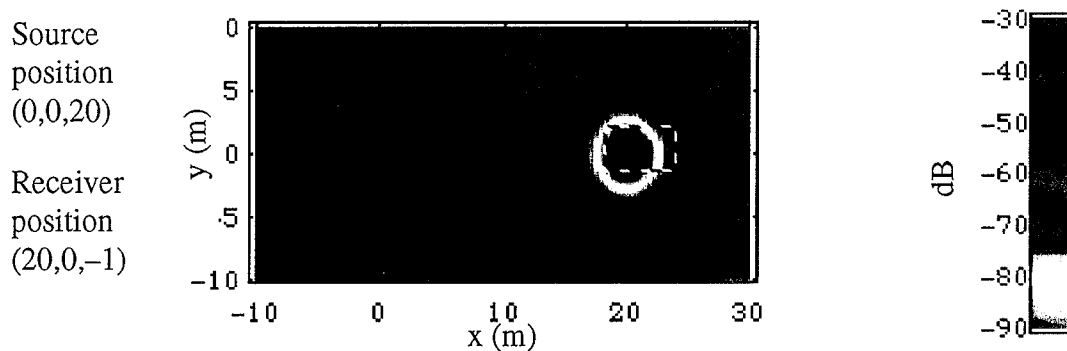


Figure 16. Scattering strength of Figure 14 minus α_b (see Eq. 7) times distance traveled from each surface position to the receiver. The result indicates the major region of the surface contributing to the received energy. All values below -90 dB have been set equal to -90 dB. As in Figure 14, higher resolution is needed to see the structure above the receiver.

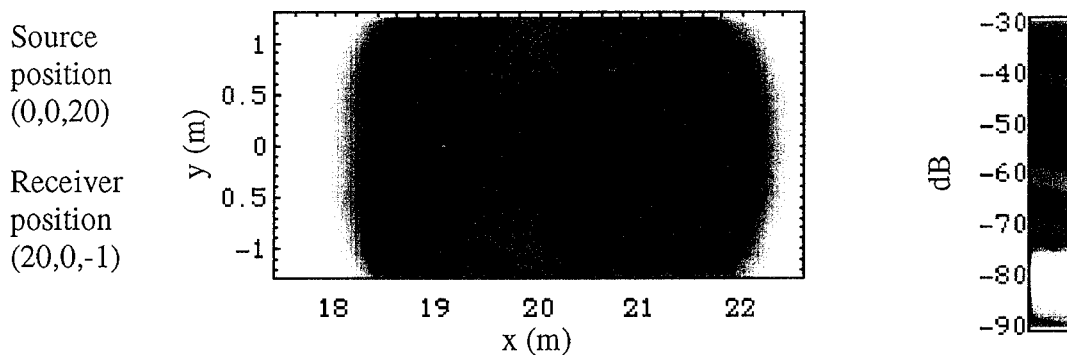


Figure 17. A high-resolution view of the boxed region in Figure 16.

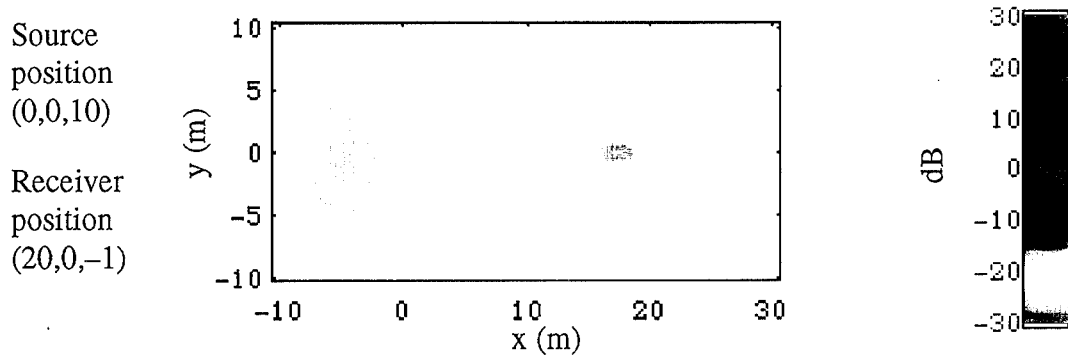


Figure 18. Scattering strength at 40 kHz as a function of position for source and receiver positions given in meters at left (x,y,z), Arafura site.

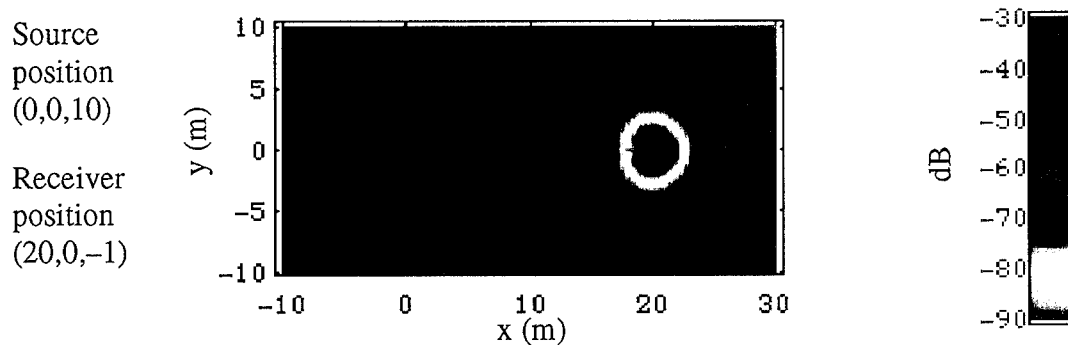


Figure 19. Scattering strength of Figure 18 minus α_b (see Eq. 7) times distance traveled from each surface position to the receiver. The result indicates the major region of the surface contributing to the received energy. All values below -90 dB have been set equal to -90 dB.

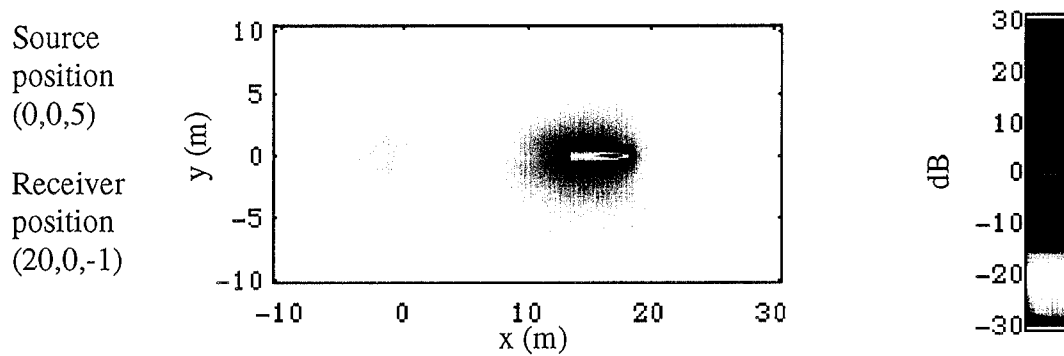


Figure 20. Scattering strength at 40 kHz as a function of position for source and receiver positions given in meters at left (x,y,z) , Arafura site.

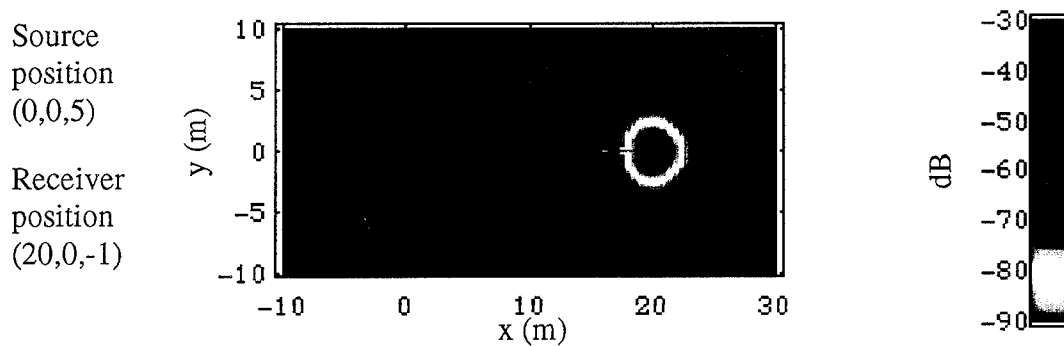


Figure 21. Scattering strength of Figure 20 minus α_b (see Eq. 7) times distance traveled from each surface position to the receiver. The result indicates the major region of the surface contributing to the received energy. All values below -90 dB have been set equal to -90 dB.

When the source is 20 and 10 m above the surface (Figures 9 and 11), the refracted path in the sediment is short enough that it contributes to the received signal. However, when the source is at 5 m above the surface (Figure 13), the contribution via the refracted path has undergone so much attenuation as to be unimportant at the receiver. The numerical results reflected in Figure 13 indicate that the primary physics contributing to the received intensity is diffraction, due to surface roughness, as calculated via surface perturbation theory.

Figures 14, 18, and 20 show the scattered strength as a function of position for source heights of 20, 10, and 5 m, respectively, for the Arafura site. For this site, the elliptical regions of maximum intensity scattered into the sediment are much narrower (see Figures 5–7 and the discussion in Section 4.1). In the case of Figure 14, in fact, a higher-resolution plot (Figure 15) is needed to see the region in the vicinity of the receiver. Again, it is useful to compare the scattered strengths (Figures 14, 18, and 20) with the contributions to the intensity seen at the receiver (Figures 16, 19, and 21). In all cases, there is a significant contribution along the refracted path. For this site, the sound speed in the sediment is less than that in the water, so no critical angle exists. As in the Quinault case, much of the received intensity comes from above the receiver. In this case, however, the received intensity is due to scattering from volume inhomogeneities, as calculated via volume-perturbation theory.

4.3 Experimental Tests of Scattering Strength Model

Moe et al. (1995) used the surface-perturbation model of Section 3.1.2 to examine the experimental results of Chotiros (1995). The results could, with certain assumptions about the surface roughness spectrum, be explained using the model. As such, Chotiros's experiment represents a consistency test of at least one aspect of the present model with real data. However, it does not demonstrate that surface perturbation is the only physics contributing to the experimental results. Chotiros has shown that the experimental results are also consistent with a Biot slow wave propagating in the sediment.

The geometries of Figures 8–21 were chosen with an experimental test of this model in mind. A field experiment is feasible in which the environmental parameters used in the model and the intensity at buried receivers are measured. Obtaining statistical results will require that the source in the water be movable. An experiment of this type has recently been proposed.

5. SUMMARY AND FUTURE DIRECTIONS

The model presented here for scattering into the sediment includes effects of both surface roughness and volume inhomogeneities. It closely follows the development of Jackson (1993). It is anticipated that in the long term the Kirchhoff and surface-perturbation theory parts of the model could be replaced with the more robust small-slope approximation (Thorsos and Broschat, 1995). Likewise, as more computational power becomes available, it would seem feasible to replace the treatment of the volume scattering as an equivalent surface effect with a more ambitious calculation of scattering within the sediment volume.

Having said this, the model, as developed to this point, seems to capture many of the effects one might anticipate as well as at least one (subcritical penetration) that might not be so obvious. Quantitative testing of the model awaits further experiments.

6. REFERENCES

- Chotiros, N.P., 1995: "Biot model of sound propagation in water-saturated sand," *J. Acoust. Soc. Am.* **97**, 199–214.
- Hamilton, E.L., and R.T. Bachman, 1982; "Sound velocity and related properties of marine sediments," *J. Acoust. Soc. Am.* **72**, 1891–1904.
- Jackson, D.R., and K.B. Briggs, 1992: "High-frequency bottom backscattering: Roughness versus sediment volume scattering," *J. Acoust. Soc. Am.* **92**, 962–977.
- Jackson, D.R., 1993: "A Model for Bistatic Bottom Scattering in the Frequency Range 10–100 kHz," Technical Report 9305, Applied Physics Laboratory, University of Washington, August 1993.
- Moe, J. E., E. I. Thorsos, D. R. Jackson, and K. L. Williams, 1995: "The effect of roughness on acoustic penetration of the seafloor as given by a fluid–fluid perturbation model and comparison with recent sediment penetration experiments," *J. Acoust. Soc. Am.* **97**, 3315–3316.
- Mourad, P.D., and D.R. Jackson, 1989: "High frequency sonar equation models for bottom backscatter and forward loss," in *Proceedings of OCEANS '89* (IEEE, New York), pp. 1168–1175.
- Richardson, M. D., and K. B. Briggs, 1993: "On the use of acoustic impedance values to determine sediment properties," in *Acoustic Classification and Mapping of the Seabed*, N. G. Pace and D. N. Langhorne, Eds (Institute of Acoustics, Bath), pp. 15–25.
- Thorsos, E. I., and S. L. Broschat, 1995: "An investigation of the small slope approximation for scattering from rough surfaces. Part I. Theory," *J. Acoust. Soc. Am.* **97**, 2082–2093.
- Yaglom, A.M., 1962: *An Introduction to the Theory of Stationary Random Functions* (Prentice-Hall, Englewood Cliffs, N.J.).

APPENDIX

Definition of Bistatic Cross Section

Typically the bistatic cross section is defined as

$$\sigma = \frac{r^2 I_s}{A I_i}, \quad (\text{A1})$$

where r is the range from the scattering point on the surface to the receiver, I_s is the scattered intensity measured at r , A is the patch of the surface contributing to I_s , and I_i is the incident intensity. However, in the present case, the effect of attenuation in the sediment is taken into account in addition to the effect of spherical spreading. Thus the definition of cross section used here is

$$\sigma = \frac{r^2 (e^{2\delta k_{br} r}) I_s}{A I_i}, \quad (\text{A2})$$

where the factor in parenthesis accounts for the attenuation in the sediment, k_{br} is the real part of the acoustic wavenumber in the sediment (see text below Eq. 3), and δ is defined in Table 1. This definition then leads to correct calculations of intensity received in the sediment when attenuation is included in that calculation.

Distribution List For

APL-UW TR 9505

NAVY AGENCIES

Office of Naval Research

Ballston Towers 1
800 North Quincy Street
Arlington, VA 22217-5660

Attn: Code 321OA (Edward Chaika)
321OA (Edward Estalote)
321OA (Jeffrey Simmen)
321TS (Wallace Ching)
321TS (Randall Jacobson)
322GG (Joseph Kravitz)
322PO (Louis Goodman)
322TE (Barry P. Blumenthal)

NAVY LABORATORIES

Commanding Officer

Naval Research Laboratory

4555 Overlook Avenue, S.W.
Washington, DC 20375-5000

Attn: Code 5200 Library

Commanding Officer

Naval Research Laboratory

Detachment Stennis Space Center

Stennis Space Center, MS 39529-5004

Attn: Code 7170 (Roger W. Merideth)
7170 (Dan J. Ramsdale)
7333 (Kevin G. Briggs)
7430 (Samuel G. Tooma)
7431 (Michael D. Richardson)

Commanding Officer

Naval Surface Warfare Center

Coastal Systems Station

6703 West Highway 98
Panama City, FL 32407-7001

Attn: Code E29 Technical Library
Code 10M (Elan Moritz)
130B (Raymond Lim)
130B (Joseph L. Lopes)
130B (Gary S. Sammelman)
130B (Cynthia C. Weilert)
3110 (Kerry W. Commander)
3110 (Robert V. Croft)
3110 (William C. Littlejohn)

Commander

Naval Undersea Warfare Center

Division Newport

1176 Howell Street
Newport, RI 02841-1708

Attn: Code 0262 Technical Library
842 (Frank E. Aidala, Jr.)
8423 (John R. Ventura)

Naval Undersea Warfare Center

New London Detachment

New London, CT 06320-5594

Attn: Library
Code 3122 (Henry Weinberg)

UNIVERSITY LABORATORIES

The Pennsylvania State University

Applied Research Laboratory

P.O. Box 30
State College, PA 16804-0030

Attn: Lee Culver
Ralph Goodman

University of California, San Diego

Scripps Institution of Oceanography

Marine Physical Laboratory, 0701

P.O. Box 6049
San Diego, CA 92166-6049

Attn: William Kuperman, Director
William S. Hodgkiss

University of Texas at Austin

Applied Research Laboratory

P.O. Box 8029
Austin, TX 78713-8029

Attn: Nicholas P. Chotiros

INDUSTRY AND CONSULTING AGENCIES

Planning Systems Inc.

7923 Jones Branch Drive
McLean, VA 22102

Attn: Charles W. Holland

Science Applications International Corporation (SAIC)

P. O. Box 658
Mashpee, MA 02649

Attn: Ruth Keenan

REPORT DOCUMENTATION PAGE

Form Approved
OPM No. 0704-0188

Public reporting burden for this collection of information is estimated to average 1 hour per response, including the time for reviewing instructions, searching existing data sources, gathering and maintaining the data needed, and reviewing the collection of information. Send comments regarding this burden estimate or any other aspect of this collection of information, including suggestions for reducing this burden, to Washington Headquarters Services, Directorate for Information Operations and Reports, 1215 Jefferson Davis Highway, Suite 1204, Arlington, VA 22202-4302, and to the Office of Information and Regulatory Affairs, Office of Management and Budget, Washington, DC 20503.

1. AGENCY USE ONLY (Leave blank)		2. REPORT DATE November 1995	3. REPORT TYPE AND DATES COVERED Technical
4. TITLE AND SUBTITLE A Model for Bistatic Scattering into Ocean Sediments for Frequencies from 10 – 100 kHz			5. FUNDING NUMBERS N00039-91-C-0072
6. AUTHOR(S) Kevin Williams and Darrell Jackson			
7. PERFORMING ORGANIZATION NAME(S) AND ADDRESS(ES) Applied Physics Laboratory University of Washington 1013 NE 40th Street Seattle, WA 98105-6698			8. PERFORMING ORGANIZATION REPORT NUMBER APL-UW TR 9505
9. SPONSORING / MONITORING AGENCY NAME(S) AND ADDRESS(ES) Naval Coastal Systems Station Panama City, FL 32407-5000			10. SPONSORING / MONITORING AGENCY REPORT NUMBER
11. SUPPLEMENTARY NOTES			
12a. DISTRIBUTION / AVAILABILITY STATEMENT Approved for public release; distribution unlimited.			12b. DISTRIBUTION CODE
13. ABSTRACT (Maximum 200 words) A model is developed for bistatic scattering into ocean sediments by an acoustic source located in the water and a receiver buried in the bottom. The model is closely related to that developed by Jackson (1993) for a source and receiver that were both located in the water and parallels that effort in many regards. In particular, bottom scattering is treated as being due to interface roughness and volume inhomogeneity. Kirchhoff theory is used to explain interface scattering near the refracted (Snell's law) direction, and perturbation theory (Moe et al., 1995) is used for all other directions. Perturbation theory is used to treat the scattering due to volume inhomogeneities. Model results are presented for two of the bottom sites examined by Jackson (1993), and possible experimental tests of the model are discussed briefly.			
14. SUBJECT TERMS Acoustic sediment scattering, in-sediment scattering strength, high-frequency environmental acoustics			15. NUMBER OF PAGES 36
			16. PRICE CODE
17. SECURITY CLASSIFICATION OF REPORT Unclassified	18. SECURITY CLASSIFICATION OF THIS PAGE Unclassified	19. SECURITY CLASSIFICATION OF ABSTRACT Unclassified	20. LIMITATION OF ABSTRACT SAR